Second International Symposium on Marine Propulsors
smp'11, Hamburg, Germany, June 2011
Workshop: Cavitation on foil

Cavitation Prediction of Flow over the Delft Twist 11 Foil

Stewart Whitworth[1]

[1]Technical Investigation Department (TID), Lloyd's Register, London, UK

ABSTRACT

The periodic cavity shedding observed in cavitation tunnel tests for flow over the Delft Twist 11 foil has been successfully predicted by CFD analysis. The RANS turbulence models implemented in STAR-CCM+, a commercial CFD solver, have been shown to be inadequate for modelling such a problem, which was instead solved using a DES model. The highly dynamic cavitation pattern and the collapses occurring within it resulted in extreme pressures on the surface of the foil causing the instantaneous lift and drag forces to vary greatly.

Keywords

Delft, foil, CFD, cavitation, DES

1 INTRODUCTION

Cavitation is a serious concern for the marine industry not only because of the noise, vibration and erosion problems it can cause but also because, until recently, it has not been possible to accurately predict its behaviour, and, therefore, prevent such problems from occurring. Recent increases in available computational resources and improvements in turbulence modelling capabilities mean that now, with the correct tools and knowledge, cavitation can be predicted reliably and accurately. This paper will demonstrate that this is the case by modelling cavitating flow over the Delft Twist 11 foil, a three-dimensional small-scale foil for which considerable experimental data is available.

2 PROCEDURE

All simulations were performed using STAR-CCM+ 6.02.007, a commercial, finite-volume solver for flow, thermal and stress analysis (CD-adapco 2011). For all calculations the flow velocities and pressures in the domain are calculated using the standard SIMPLE (Semi Implicit Method for Pressure Linked Equations) pressure correction method. A second-order upwind differencing scheme was employed for the solution of the momentum and turbulence equations. Second-order temporal discretisation was used.

2.1 Foil Geometry

The Delft Twist 11 Foil is a wing of rectangular planform, the section shape being uniform over the whole span, but the orientation with respect to the incoming flow varying in spanwise direction. The section shape is a modified symmetrical NACA 4-digit profile and the spanwise angle of attack varies between -2° at the wall of the tunnel and 9° at the midsection. It has a span of 0.3m and a chord length of 0.15m.

2.2 Computational Domain

The computational domain extended four chord lengths (0.6m) aft of the foil's trailing edge and two chord lengths (0.3m) forward of its leading edge. Flow was modelled around half of the foil with a plane of symmetry applied along its midsection. The other external boundaries were modelled as free-slip walls and the inflow and outflow were applied as uniform velocity inlet and pressure outlet boundaries.

2.3 Case Summary

Two cases were simulated representing experiments performed in the cavitation tunnel at Delft University of Technology. These experiments were identical except for the ambient pressure in the tank, which was high enough to ensure cavitation did not occur in the first case, and low enough to ensure that it would in the second. The flow conditions are summarised in **Table 1**.

	Case 1	**Case 2**
Inflow Speed (m/s)	6.97	
Outlet Pressure (kPa)	97	29
Water Density (kg/m^3)	998	
Vapour Pressure (kPa)	n/a	2.97
Vapour Density (kg/m^3)	n/a	0.023

Table 1 – Flow Conditions

2.4 Meshing

All meshes employed were either polyhedral or predominantly-hexahedral trimmed unstructured grids incorporating a prism layer mesh around the foil and were generated in STAR-CCM+.

Non-cavitating preliminary investigations were performed to optimise the prism layer mesh for a "high y+" (i.e. wall function) approach, obtaining a mean y+ of 27.2 and a max y+ of 61.8 near the leading edge at the centre of the foil, as shown in **Figure 1**.

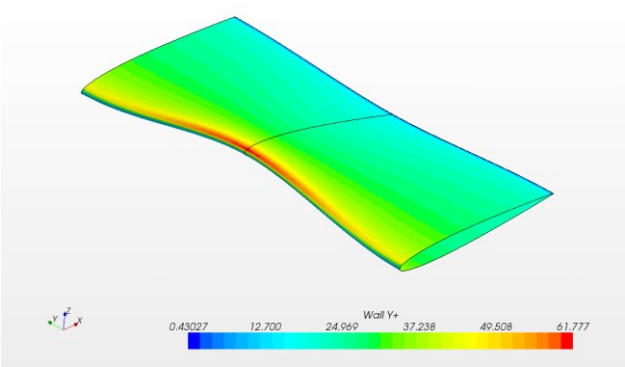

Figure 1 – Wall y+ on the foil with the mesh optimised for a wall function approach.

Much finer "low y+" prism layer meshes were also generated but the increasingly high aspect ratio of the near-wall cells meant that it was not possible to refine the prism layer sufficiently to fully resolve the boundary layer whilst still obtaining a well-converged solution. Since further volume refinement was considered likely to lead to meshes too fine to be practical at this stage, "high y+" prism layer settings were chosen for use in subsequent analyses.

Non-cavitating grid convergence studies were performed using a total of 12 trimmed and polyhedral grids and the forces on the foil were analysed in order to assess grid independence and uncertainty. The key parameters of the meshes are given in **Table 2**. The 12 meshes were of three types (1p-4p, 5p-8p and 5t-8t), with the only difference between the meshes of each type being the base size parameter. Polyhedral meshes 5p-8p were broadly similar to their corresponding meshes 1p-4p with some additional refinement near the leading and trailing edges. The trimmed meshes 5t-8t were created using identical mesh settings and refinement regions as polyhedral meshes 5p-8p yet the cell size restrictions of an octree-type mesh generation process mean that certain parts of the mesh close to the foil were finer for the trimmed cell meshes than their polyhedral counterparts, resulting in a cell count ~40% greater. By way of example, mesh 6t is shown in **Figure 2**.

Mesh	Base Size	Type	# Cells (mil.)
1p	25	polyhedral	1.17
2p	20	polyhedral	1.93
3p	15	polyhedral	3.9
4p	10	polyhedral	11.4
5p	25	polyhedral	1.2
6p	20	polyhedral	2.12
7p	15	polyhedral	4.6
8p	10	polyhedral	14.03
5t	25	trimmed	1.68
6t	20	trimmed	3.06
7t	15	trimmed	6.43
8t	10	trimmed	19.33

Table 2 – Summary of meshes employed for Case 1

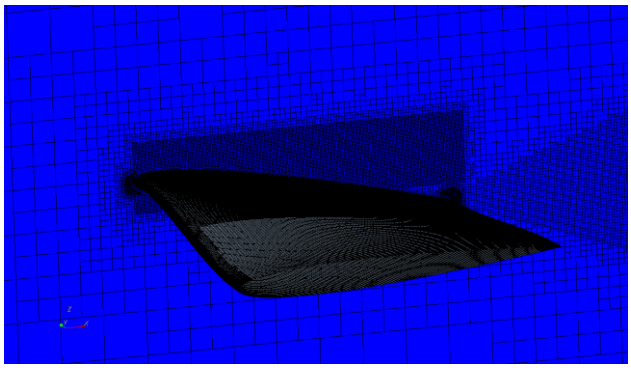

Figure 2 – Mesh around foil for mesh 6t

Trimmed-cell meshes were employed for the cavitating analyses. These were loosely based upon the medium density (base size = 20) mesh employed for the non-cavitating flows but with additional anisotropic refinement in the region where cavitation was expected and with some of the mesh further from the foil, particularly in the wake, coarsened to prevent the mesh size from becoming too great. Three meshes were employed, with the only differences between them being additional refinement to account for aspects of the cavitating flow, as described in more detail in the Results and Discussion sections. A summary of the three meshes is given in **Table 3** and mesh A is shown in **Figure 3**.

Mesh	Type	# Cells (mil.)
A	trimmed	3.71
B	trimmed	3.92
C	trimmed	4.74

Table 3 - Summary of meshes employed for Case 2

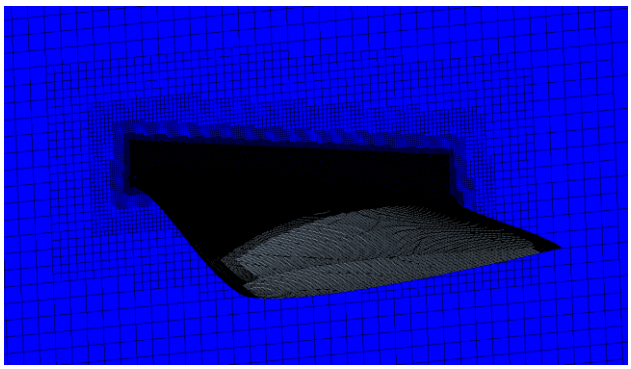

Figure 3 – Mesh around foil for mesh A

2.5 Physics

For ease of setup, all cases were solved as two-phase flows with the calculation of the phases performed using the volume-of fluid (VOF) method. For the non-cavitating case, i.e. those with the outlet close to atmospheric pressure, the VOF solver was frozen to minimise unnecessary computational expense. For the cavitating case, cavitation was modelled using the model proposed by Sauer (2000) based on a simplified Rayleigh-Plesset equation.

For the non-cavitating case, turbulence was modelled using the k-ω SST model (Menter, 1994). For the cavitating case, various turbulence models were tested, including the k-ω SST model, the realisable k-ε model (Shih et al, 1995), the cubic k-ε model (Lien et al, 1996), the Reynolds stress model (with both linear and quadratic pressure-strain terms) (Gibson & Launder, 1978, Speziale et al, 1991) and a DES model using the k-ω SST model in the free stream and the boundary layer (Menter & Kuntz, 2003). Wall treatment was performed using the shear-driven two-layer approach of Wolfstein (1969) for the k-ε model and a "high y+" (i.e. wall function) approach for the other RANS models. All turbulence model constants were left as defined by default in STAR-CCM+.

2.6 Convergence and Run Details

All analyses were performed on a 64-bit Linux cluster on between 8 and 40 CPUs. For the steady analyses, convergence was monitored both via the reduction of the normalised residuals to below 10^{-4} for continuity, momentum and turbulence equations, and the convergence of the forces to within the accuracy in which they are defined in the results. Default under-relaxation factors of 0.7 for momentum, 0.3 for pressure, 0.8 for turbulence and 0.9 for VOF were used.

The transient analysis were performed with a time step of 50μs when using RANS turbulence models and 10 μs when using the DES turbulence model. These time steps were selected by successively reducing the time step until the residuals, monitored forces and field pressures at selected locations were converging within 5 iterations per time step when using under-relaxation factors of 0.9 for momentum, 0.5 for pressure, 0.8 for turbulence and 0.9 for VOF. Checks were made to ensure that further time step reductions did not have a noticeable effect on the monitored forces, pressure coefficients and cavitation volume.

3 RESULTS

3.1 Case 1 – Flow Without Cavitation

Estimated lift and drag values for infinitely fine meshes were obtained via linear extrapolation and uncertainties were calculated using the method described by Eça et al (2010) and the "base size" parameter, upon which all cell dimensions bar those regarding prism layer thickness were based. The lift and drag forces obtained from these analyses are given in **Table 4** and shown in **Figure 4** and **Figure 5**.

Mesh	Lift (N)	Drag (N)
1p	232.7	8.37
2p	232.8	8.31
3p	232.5	8.23
4p	232.4	8.15
5p	233	8.36
6p	233.2	8.29
7p	232.8	8.21
8p	232.8	8.12
5t	232.6	8.49
6t	232.7	8.44
7t	232.9	8.37
8t	233.2	8.34

Table 4 – Lift and drag forces for Case 1

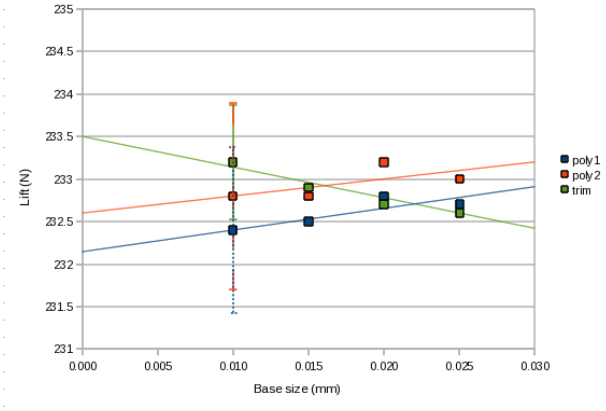

Figure 4 – Lift forces on the foil for the 12 meshes employed for Case 1

Bar a small amount of scatter the lift force is the same on all meshes, 232.8N ± 0.2%, with pressure forces comprising over 99.99%. The extrapolation to infinite mesh density and the uncertainty analysis (indicated by error bars in **Figure 4**) give a potential range for the lift of 232.7N ± 0.5%.

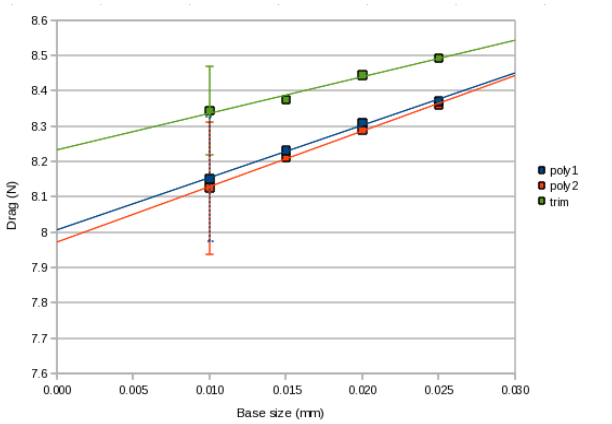

Figure 5 – Drag forces on the foil for the 12 meshes employed for Case 1

Unlike the lift force, the much smaller drag force reduces as the mesh density increases. There is a significant (2.7%) difference between the drag results on the finest trimmed mesh (mesh 8t) and those obtained on the finest polyhedral mesh (mesh 8p). The extrapolations imply drag values of 8.24N on an infinitely fine trimmed mesh and 7.98-8.01N on an infinitely fine polyhedral mesh. The potential range derived from the uncertainty analysis is 7.94-8.47N. Pressure and shear drag forces for the finest trimmed mesh are 3.53N and 4.82N, respectively. For the finest polyhedral mesh, these are 3.34N and 4.78N, respectively.

The maximum pressure coefficient on the foil was 1.02 for all meshes. The minimum pressure coefficient varied between -3.18 and -3.13, reducing as the mesh density increased. The estimated minimum pressure coefficient for an infinitely fine mesh is -3.18 ± 1.0%.

Streamlines on the pressure an suction side of the foil, as calculated on mesh 8p, are shown in **Figure 6**. No significant differences could be seen between these and the streamlines on the other meshes.

3.2 Case 2 – Flow With Cavitation

3.2.1 RANS turbulence models

The cavitating flow was initially simulated on mesh A. The acceptability of this mesh was proven by first performing a single-phase analysis and comparing the drag and lift forces and maximum and minimum pressure coefficients with those obtained on the earlier meshes. These were 8.20N, 233.2N, 1.02 and -3.21, respectively, all of which are within the ranges calculated in section 4.1.

Using the k-ω SST turbulence model, the cavitating analysis produced a predominantly-stable sheet cavity along the leading edge, across roughly the central two-thirds of the span and shaped not dissimilarly to that observed on the Twist 11 foil (**Figure 7**). However, contrary to the experimental observations, no shedding was predicted.

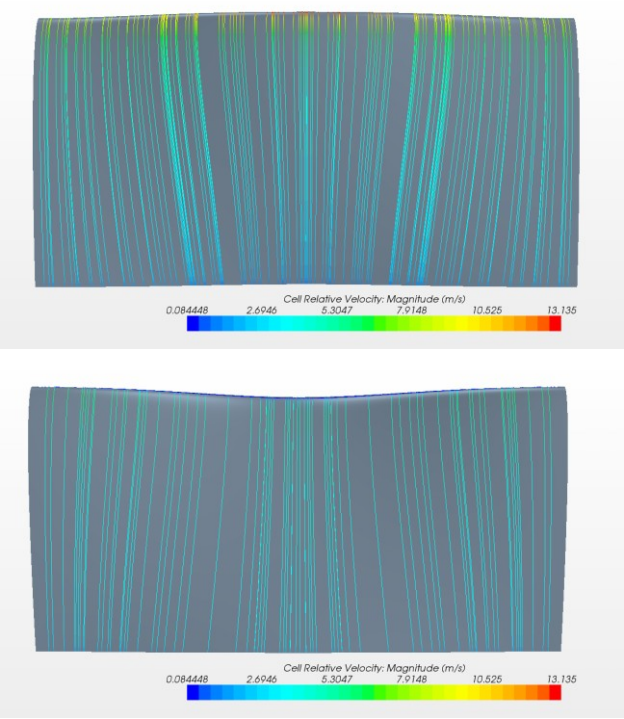

Figure 6 – Streamlines on suction (top) and pressure sides of the foil, as calculated on mesh 8p.

Figure 7 – Stable sheet cavity on foil when using the k-ω SST turbulence model

Simulations performed on mesh A using the realisable k-ε model and the cubic k-ε model yielded very similar results to those obtained using the k-ω SST model (**Figures 8** and **9**, respectively), again with no cavity shedding occurring.

Figure 8 – Stable sheet cavity on foil when using the realisable k-ε turbulence model

Figure 9 – Stable sheet cavity on foil when using the cubic k-ε turbulence model

For the analyses employing the Reynolds stress model (RSM) to not diverge, a finer mesh was required near the trailing edge. The cavitation patterns obtained on this mesh, mesh B, using the RSM variants with linear and quadratic pressure-strain terms are shown in **Figures 10** and **11**, respectively.

Figure 10 – Stable sheet cavity on foil when using the linear Reynolds stress turbulence model

Figure 11 – Unstable sheet cavity on foil when using the quadratic Reynolds stress turbulence model

The cavitation pattern obtained with the linear Reynolds stress model was broadly similar to those obtained with the two-equation RANS models: a predominantly stable sheet cavity across the central two-thirds of the leading edge. By contrast, the pattern obtained with the quadratic Reynolds stress model was highly unstable. Despite initially shedding cavitation, the instability of the cavitation also led to instability in the solver and it proved impossible to prevent it from diverging within a few hundredths of a second, regardless of the initial conditions.

In the four RANS analyses for which a converged solution was obtained, the sheet cavity was not fully stable but rather pulsated with a regular frequency. These frequencies are given in **Table 5** along with mean calculated cavitation volumes and their amplitudes. Mean drag and lift forces, maximum and minimum pressure coefficients and their amplitudes are given in **Table 6**.

Turbulence Model	**Oscillation Frequency (Hz)**	**Cavitation Volume (x10^{-6} m^3)**		
		Integral[1]	**Cells σ > 0.5[2]**	**Cells σ > 0.05[3]**
k-ω SST	90.1	2.61 ± 0.02	2.55 ± 0.15	4.14 ± 0.42
realisable k-ε	31.4	3.30 ± 0.16	3.34 ± 0.15	4.85 ± 0.23
cubic k-ε	91.7	3.02 ± 0.01	3.07 ± 0.04	4.40 ± 0.16
Linear RSM				

Table 5 – Oscillation frequencies and cavitation volumes calculated using RANS turbulence models
[1] Integration of the vapour volume fraction
[2] Volume of all cells with vapour volume fraction > 0.5
[3] Volume of all cells with vapour volume fraction > 0.05

Turbulence Model	Drag (N)	Lift (N)	max Cp	min Cp
k-ω SST	13.06 ± 0.21	222.7 ± 1.9	1.022 ± 0.004	-1.240 ± 0.015
realisable k-ε	13.05 ± 0.55	227.2 ± 3.9	1.031 ± 0.014	-1.238 ± 0.015
cubic k-ε	13.07 ± 0.07	220.4 ± 0.8	1.022 ± 0.002	-1.235 ± 0.010
Linear RSM	13.22 ± 0.07	220.4 ± 0.8	1.013 ± 0.001[1]	-1.238 ± 0.012[1]

Table 6 - Forces and pressure coefficients calculated using RANS turbulence models

[1] When using the linear, spikes are observed in the pressure coefficients outside of the ranges quoted

3.2.2 Detached eddy simulation (DES)

Modelling the turbulent flow using detached eddy simulation (DES) required the mesh to be refined further in the cavitating part of the flow on the suction side of the foil. In order to ensure that the cavitation didn't "explode" and the analysis diverge, particular attention to the quality and refinement of the mesh was required near to the leading edge. Mesh C was the result of this refinement and comprised 4.74 million cells. The cells in the region where cavitation was expected to occur were roughly 1mm in the spanwise direction, 0.5mm in the chordwise direction and 0.25mm in the vertical direction. **Figure 10** shows a measure of the blending between the RANS and **Figure 10** shows the cells in which the LES model is active, which are all close to the suction side of the foil. The RANS model operates in the 60% of cells that comprise the remainder of the domain.

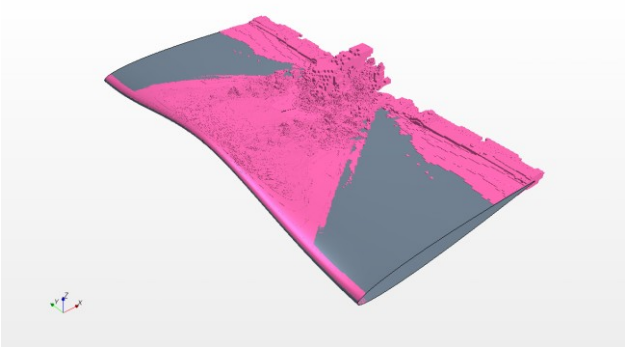

Figure 10 – Blending of the DES model at one instant in time

The cavitation pattern obtained using DES was considerably different from those predicted using the RANS turbulence models. Whilst the sheet cavity remained similar in shape, the total cavitation volume was considerably greater and the cavity would regularly shed a large, and highly turbulent cloud, which would gradually collapse as it moved aft. **Figure 11** shows three snapshots of the shedding cycle alongside stills taken from the movie of the experiment. For clarity, negative images are used.

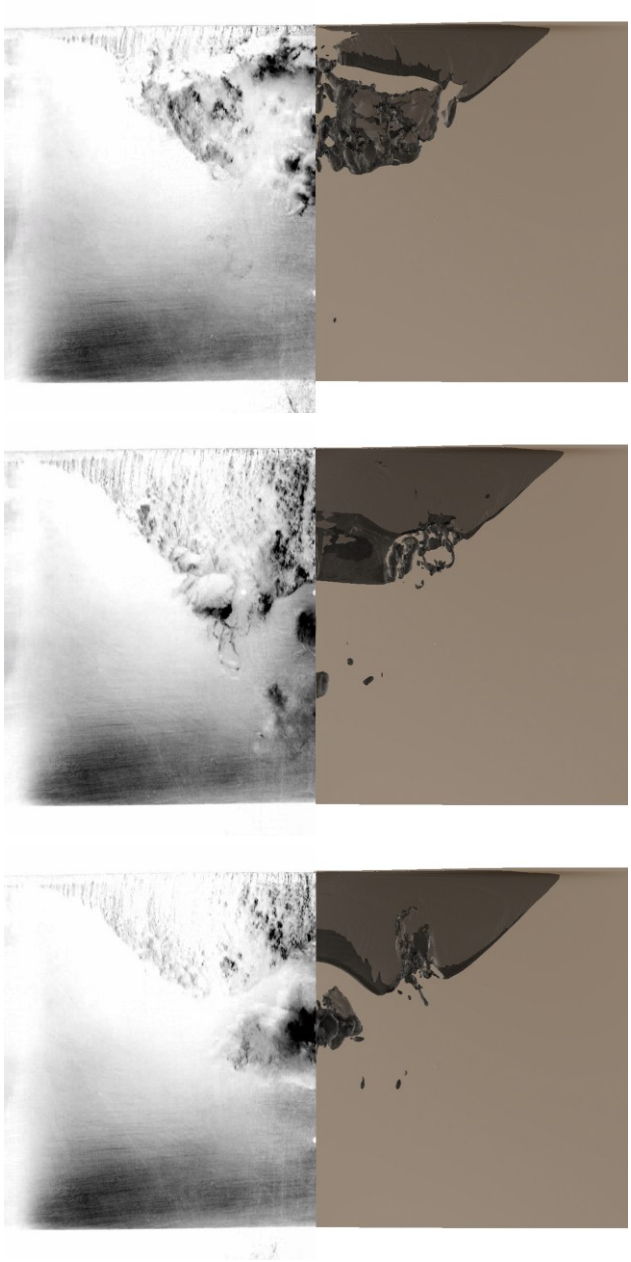

Figure 11 – Observed (left) and predicted cavitation on the suction side of the foil

The shedding of the cavitation is not identical every cycle and this leads to some variation in the shedding frequency between 32Hz and 38Hz, when measured peak-to-peak on the cavitation volume history. A section of this is shown in **Figure 12** along with its FFT in **Figure 13**. The FFT shows a peak for the shedding frequency at 35±2.5Hz. The short length of the usable data sample (0.42s) means that the FFT is not well enough resolved to give a more precise estimate.

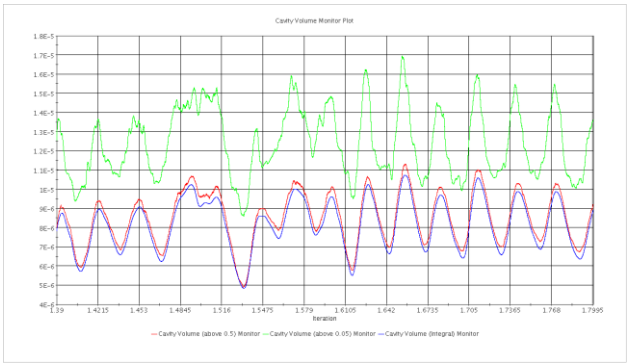

Figure 12 – Cavitation volume time history

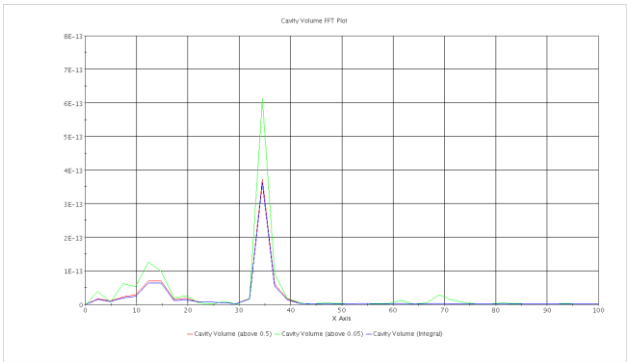

Figure 13 – Cavitation volume time history FFT

The monitored forces, pressure coefficients and cavitation volumes are summarised in **Table 7**. **Figure 14** shows a section of the time history of the maximum pressure coefficient on the foil. **Figure 15** shows the drag force over the same time period.

		Range	Mean
Drag (N)		-43.2 – 19.6	13.7
Lift (N)		74.5 – 284.5	233.2
max Cp		0.896 – 84.02	1.41
min Cp		-9.47 – -1.22	-1.24
Cavitation Volume ($x10^{-6}$ m^3)	**Integral**	4.52 – 10.72	8.15
	Cells σ > 0.5	4.90 – 11.31	8.50
	Cells σ > 0.05	8.00 – 16.95	12.42

Table 7 – Monitored forces, pressure coefficients and cavitation volumes from DES analysis

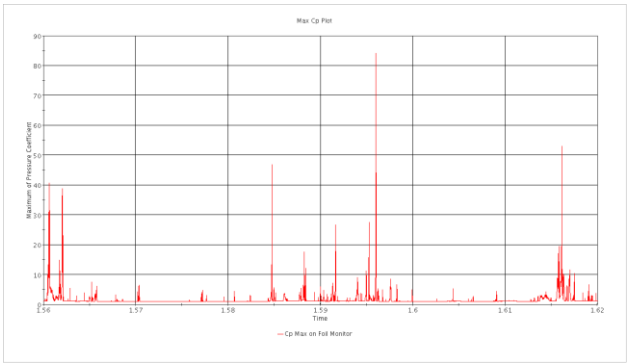

Figure 14 – Maximum pressure coefficient time history

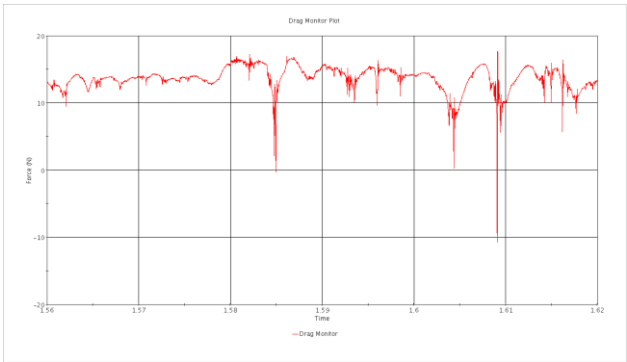

Figure 15 – Drag force time history

Streamlines on the two sides of the foil at a particular instant in time are shown in **Figure 16**. A translucent isosurface of the cavitation is included.

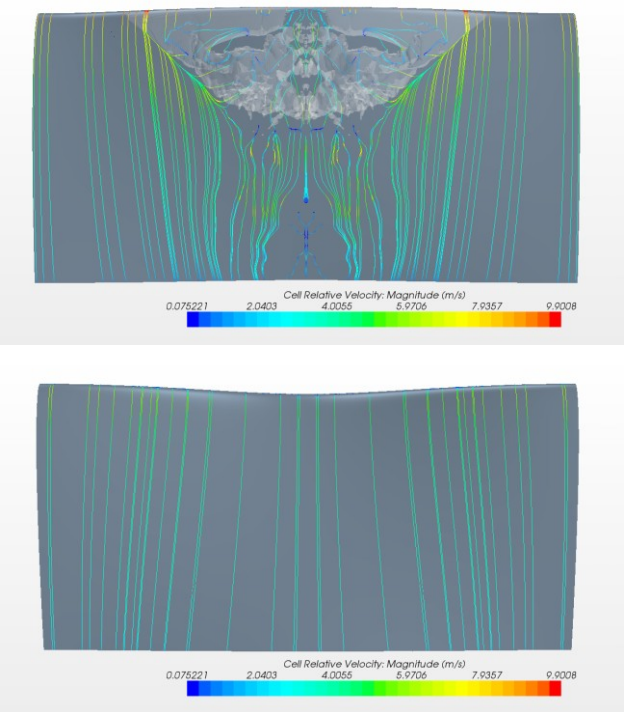

Figure 16 – Streamlines on suction (top) and pressure sides of the foil

4 DISCUSSION

4.1 Case 1 – Flow Without Cavitation

The calculated lift and drag forces seem reasonable and the consistency of the trends when the meshes were refined methodically is as one would expect. However, the difference in the predicted drag between the trimmed meshes and the polyhedral meshes is of concern and cannot easily explained. Since the discrepancy is more due to pressure forces than shear forces, it was assumed that this was most likely due to different pressures being predicted at the leading edge and this indeed was the case. The high pressure gradients near the leading edge mean that accurate prediction of the separation line will be paramount and this will be dependent on both turbulence modelling and mesh resolution. Whilst very fine meshes at the leading edge should remove the disparity between the two mesh types, it is suspected that the trimmed meshes are providing the more accurate prediction for two reasons. Firstly, and most simply, they are finer and secondly, previous experience has shown that the improved mesh-flow alignment of such orthogonal meshes can provide increased accurate for predominantly monodirectional flows such as this one.

The maximum and minimum pressure coefficients also appear reasonable and the streamlines conform with expectations.

4.2 Case 2 – Flow With Cavitation

The failure of the RANS turbulence models to predict the cavity shedding is disappointing and serves to emphasise their limitations for highly dynamic flows. That said, this is a phenomenon that has been documented previously, a fact that the author only discovered after these analyses had been performed. Some researchers (Li, D. et al, 2010; Li, Z. et al, 2010) have bypassed this problem by using the Reboud correction (Reboud et al, 1998) to reduce the turbulent viscosity in regions of the flow that are part-vapour, part-liquid. The author investigated the possibility of correcting the turbulent viscosity calculation along these lines but found STAR-CCM+ to be far from conducive to such modifications being made.

TID have experience of using DES to model complex cavitation patterns (Boorsma & Whitworth, 2011; Radosavljevic & Whitworth, 2010; Radosavljevic et al, 2011). However, the significantly increased overhead compared to RANS modelling means that the decision to use it is not one that should be taken lightly. For this case, the 28% increase in the size of the mesh combined with having to use a time step one-fifth of the size meant that the analysis took roughly 350 CPU-hours per shedding cycle. For a given physical duration, the DES analysis required seven times the computational effort as the analyses performed using the two-equation RANS models.

The visual correlation of the predicted and observed cavitation patterns is very good and the predicted shedding frequency, whilst variable and imprecise, matches well those reported in the experiment. The complexity of the predicted cavitation pattern is a particularly striking demonstration of the advantages of using a truly dynamic turbulence model such as DES.

The very large variation in the pressure coefficient, as shown in **Table 7** and **Figure 14**, is a consequence of highly dynamic cavitation pattern, the collapses of which result in pressure peaks of up to 2MPa, as well negative pressures as low as -200kPa. These extreme peaks are of the order of 100μs in duration and are highly irregular. They are also responsible for the large variation in the drag and lift forces. Whilst the Reynolds stress model also predicted pressure spikes, it is suspected that such phenomena would not be predicted accurately by a RANS model. The intention is to seek any experimental data that exists to confirm this prediction or, indeed, find out if the researchers who performed the experiments on this foil observed any earl signs of cavitation erosion, such as work hardening, "orange peel" or pitting, on the surface of the foil as a consequence of cavitation impacts. TID has been developing models for the prediction of cavitation erosion (Boorsma & Whitworth, 2011; Radosavljevic & Whitworth, 2010). These were not utilised in the analyses discussed here but may be applied to the present case in future work.

5 CONCLUSIONS

The following conclusions are drawn based upon this study:

- Complex, highly dynamic cavitation phenomena can be modelled accurately using CFD.
- Uncorrected RANS models are not adequate for such a task.
- DES turbulence models are better able to handle highly dynamic flows.
- Obtaining a fully grid-independent solution can require more cells than is practical, even for relatively simple problems.

REFERENCES

Boorsma, A., Whitworth, S. (2011) 'Understanding the Details of Cavitation'. Second International Symposium on Marine Propulsors (smp'11), Hamburg, Germany.

CD-adapco (2011). STAR-CCM+ 6.02.007 User Guide.

Eça L, Vaz, G. & Hoekstra, M. (2010) 'Code Verification, Solution Verification And Validation In RANS Solvers'. Proceedings of ASME 29th International Conference on Ocean, Offshore and Arctic Engineering (OMAE2010), Shanghai, China.

Gibson, M.M. & Launder, B.E. (1978) 'Ground effects on pressure fluctuations in the atmospheric boundary layer'. Journal of Fluid Mechanics Digital Archive, 86(03), 491-511.

Li, D., Grekula, M., Lindell, P. (2010) 'Towards numerical prediction of unsteady sheet cavitation on hydrofoils'. Proc. 9th International Conference on Hydrodynamics, Shanghai, China.

Li, Z., Pourquie, M., van Terwisga, T. J. C. (2010) 'A numerical study of steady and unsteady cavitation on a 2D hydrofoil'. Proc. 9th International Conference on Hydrodynamics, Shanghai, China.

Lien, F.S., Chen W.L. & Leschziner, M.A. (1996) 'Low Reynolds number eddy viscosity modelling based on non-linear stress-strain/vorticity relations'. Proc. 3rd Symp. On Eng. Turbulence Modelling and Measurements, Crete, Greece. pp. 91–100.

Menter, F. R. (1994) 'Two-Equation Eddy-Viscosity Turbulence Models for Engineering Applications'. AIAA Journal, Vol. 32, No. 8, pp. 1598-1605.

Menter, F.R. & Kuntz, M. (2003) 'Adaptation of Eddy-Viscosity Turbulence Models to Unsteady Separated Flow Behind Vehicles'. Proc. Conf. The Aerodynamics of Heavy Vehicles: Trucks, Busses and Trains, Asilomar, Ca.

Radosavljevic, D., Whitworth, S. (2010) 'Advanced CFD Techniques'. Lloyd's Register Technology Days, London.

Radosavljevic, D., Whitworth, S., Zegos, C. (2011) 'Stern Challenge – Getting It Right'. Proc. Conf. Developments in Marine CFD, RINA, London.

Reboud, J. L., Stutz, B., Coutier, O. (1998) 'Two phase flow structure of cavitation experiment and modelling of unsteady effects'. Proc. of the 3rd Int. Symp. on Cavitation, Grenoble, France.

Sauer J.(2000) Instationär kavitierende Strömungen-Ein neues Modell, basierend auf Front Capturing (VoF) und Blasendynamik. PhD thesis, Universität Karlsruhe.

T.H. Shih, W.W.Liou, A.Shabbir, Z.Yang, & J.Zhu (1995) 'A new k-e eddy viscosity model for high Reynolds number turbulent flows'. Computers and Fluids, 24, 227-238.

Speziale, C.G., Sarkar, S. & Gatski, T.B. (1991) 'Modeling the Pressure-Strain Correlation of Turbulence: an Invariant Dynamical Systems Approach'. Journal of Fluid Mechanics, Vol. 227, pp. 245-272.

Wolfstein, M. (1969) 'The velocity and temperature distribution in one-dimensional flow with turbulence augmentation and pressure gradient'. Int. J. Heat Mass Transfer, 12, pp. 301-318.